Ocean Engineering 250 (2022) 110932

Contents lists available at ScienceDirect

Ocean Engineering

journal homepage: www.elsevier.com/locate/oceaneng

Assessment and improvement of the wave generation accuracy using a wave separation method

Enrique M. Padilla [a,*], Jose M. Alsina [b]

[a] Andalusian Institute for Earth System Research (IISTA), University of Granada, Granada, Spain
[b] Laboratori d'Enginyeria Marítima, Universitat Politècnica de Catalunya, C. Jordi Girona, 1-3 08034, Barcelona, Spain

ARTICLE INFO

Keywords:
Free-wave contamination
Wave generation
Active wave absorption
Wave separation

ABSTRACT

Free-wave contamination is a non-desirable but frequent characteristic in many wave tank experiments. Higher-order wave generation is not widely implemented yet, whereas the effectiveness of active wave absorption systems is frequency-dependent, and usually unknown. The resulting free-wave contamination usually remains unnoticed, but may have important consequences especially at low frequencies. We present a Generation–Separation–Compensation (GSC) procedure to identify, quantify and attenuate the free-wave contamination. The resulting wave field behaves as expected from a higher-order wave generation with no re-reflections at the wave paddle. The attenuation ratio of the unwanted energy content is relatively high (between 60% to 90%).

The GSC procedure uses the general framework for wave separation proposed by Padilla and Alsina (2020) with an array of in-line probes. The application of this technique over experimental data is presented with excellent results. The robustness of the qualitative analysis is guaranteed for experimental settings fulfilling a minimum distance between the first and the last probe and a maximum spacing between probes. The stability of the quantitative analysis is guaranteed when P, number of probes forming the array, is above five, and $\Delta x_{sep}/\lambda$, ratio between the spacing of the probes forming the array and the wavelength, is within the recommended range 0.1–0.45.

1. Introduction

In many experimental studies, a high control of the wave conditions is fundamental, i.e., the target wave field being accurately generated. However, wave generation systems present many difficulties to accurately reproduce the target wave field (Hansen and Svendson, 1974; Hansen et al., 1980; Madsen and Sørensen, 1993; Schäffer, 1996; Van Dongeren et al., 2002).

First-order wave-generation systems cannot accurately reproduce nonlinear wave fields (Barthel and Mansard, 1988). When using first order wave generation, the target primary waves are generated alongside with the naturally generated superharmonic and subharmonic bound waves (self, sum and difference interaction components). The resulting wave field does not fully satisfy the linear boundary condition at the wave-maker. As a consequence, an excess of wave energy is generated at the superhamonics and subharmonics in the way of ingoing free waves (Hansen et al., 1980). These free waves are typically called *spurious waves* because of their unwanted nature. These spurious waves contribute to the free-wave contamination that enhances the differences between the measured and the target wave field (Barthel and Mansard, 1988). During the last decades, much work has been done to improve the wave generation systems above first-order. Schäffer (1996) and Van Leeuwen and Klopman (1996) formulated and implemented the wave-maker generation theory up to second-order. Spinneken and Swan (2009a), Spinneken (2010) and Aknin (2015) implemented second-order force-feedback controlled wave-maker theory, where a compensation signal is generated to cancel the spurious waves. Hence, second-order wave generations are an available technology, although not yet implemented in many of the experimental facilities around the world.

Another source of free-wave contamination is the existence of re-reflections at the wave paddle. They have been widely reported and addressed by Milgram (1965), Kostense (1984), Van Dongeren et al. (2002), Schäffer and Jakobsen (2003), Spinneken and Swan (2009a), Newman (2010) and Maguire and Ingram (2011), and many more. Regardless of the wave generation used, outgoing waves (radiated by the surf zone, reflected from testing physical models, or reflected by the shoreline) may be re-reflected at the wave paddle. These are usually called *re-reflections* and give rise to extra ingoing free waves. These

* Corresponding author.
E-mail addresses: epadilla@ugr.es (E.M. Padilla), jose.alsina@upc.edu (J.M. Alsina).

https://doi.org/10.1016/j.oceaneng.2022.110932
Received 10 December 2020; Received in revised form 18 February 2022; Accepted 21 February 2022

re-reflections are also unwanted waves and their existence is generally minimized when active wave paddle absorption is applied. Most common active wave absorption systems use measures of the surface elevation or velocities in the nearfield (Kostense, 1984; Van Dongeren et al., 2002; Schäffer and Jakobsen, 2003; Lykke Andersen et al., 2016), or measures of the force in the wave paddles (Spinneken and Swan, 2009b), to quantify the outgoing energy content. Based on this outgoing energy content, a compensating wave is generated in order to cancel out the re-reflections. However, this cancellation is not always accurate. Active wave absorption systems operate in the time domain, i.e., they cancel the re-reflections in real time. To do so, active absorption systems use digital filters (type FIR or IIR) that optimize the cancellation within the desired frequency band. Therefore, the accuracy of the absorption is frequency-dependent. For instance, the active absorption system used by Baldock et al. (2000) yield up to 90% of effective absorption for wave frequencies above 0.4 Hz, while reducing to 60% around 0.1 Hz. One of the most recent active absorption systems is the one proposed by Lykke Andersen et al. (2016). They propose a stable system based on a digital FIR filter that yields up to 90% of effective cancellation within the frequency band 0.15 Hz - 1.2 Hz for regular and irregular waves (Lykke Andersen et al., 2018).

At the wave generation stage, free-wave contamination being unnoticed may be relatively common given that the performance of the wave generation and active wave absorption systems are usually taken for granted. Unfortunately, the consequences of this unnoticed free-wave contamination may be important, e.g., a build-up of the energy at the resonance frequencies leading to deviations from the target wave field, or a build-up of low frequency seiches (Kirby et al., 2007). The latter is especially critical when testing nearshore hydrodynamics under mildly reflective environments, e.g., studies of long wave generation and propagation in shallow water (Baldock et al., 2000; Battjes et al., 2004; Padilla, 2019). For such studies, controlling the presence of free-wave contamination is critical. Orszaghova et al. (2014) reported that free-wave contamination due to first-order wave generation resulted in unrealistic excesses in the run-up distances and overtopping volumes.

In order to assess the accuracy of wave generation or wave absorption systems, the separation of the wave trains (regular in- and outgoing wave components for a target frequency) forming the regular, bichromatic or irregular wave field is a fundamental task. Many wave separation methods, such as (Goda and Suzuki, 1976; Kostense, 1984; Lin and Huang, 2004; Battjes et al., 2004; Van Dongeren et al., 2007; Lykke Andersen et al., 2017, among many others), have been proposed for the last decades with relatively good results but low degree of versatility. Padilla and Alsina (2020) (hereafter PA2020) presented a revisited and more versatile framework for wave separation in the frequency domain consisting of a qualitative and a quantitative analysis. The qualitative analysis provides useful information about the number of existing wave trains at the target frequency, the nature of these wave trains (bound or free), their propagation direction (ingoing or outgoing) and their relative importance. The quantitative analysis consists in a wave separation method to quantify the different wave trains forming the wave field at the target frequency. PA2020 tested the successful performance of this general framework with theoretical nonlinear wave cases only. A proper discussion about the applicability of this separation framework over experimental data has not been done yet. Although Alsina et al. (2016), Padilla and Alsina (2017), Padilla and Alsina (2018), Ruffini et al. (2019) and Alsina et al. (2020) have achieved good results when applying the quantitative analysis (wave separation method) to experimental wave cases.

In general terms, free-wave contamination is assumed to be a combination of limitations in the wave generation system and residual re-reflections. Regardless of the source, a procedure to identify and attenuate the free-wave contamination is still needed in most of the experimental facilities.

This paper presents a procedure to (1) identify and quantify the existing free-wave contamination (assessment of the wave generation) and (2) attenuate this free-wave contamination if needed (improvement of the wave generation). This procedure (called GSC procedure) uses the general framework for wave separation by PA2020 to assess the wave generation. When the wave generation needs improving, the GSC procedure computes the compensating waves that effectively suppress the free-wave contamination. This paper is organized as follows. Section 2 presents the GSC procedure. Section 3 summarizes the general framework for wave separation in the frequency domain. The first half of Section 4 assesses the wave generation of some experimental wave conditions (mono- and bichromatic waves). The second half addresses the improvement of the wave generation of some other wave conditions (bichromatic waves). The results are discussed in Section 5 and final remarks are given in Section 6.

2. The Generation–Separation–Compensation (GSC) procedure

In theory, the resulting wave field of an ideal wave generation consists of the following combinations of wave trains. At the primary frequencies, the expected combination is an Ingoing Free Wave (IFW), which corresponds to the linear input, and an Outgoing Free Wave (OFW) typically radiated by the surf zone, reflected from testing physical models, or reflected by the shoreline. At superharmonics or subharmonics of the primary frequencies, the expected combination is an Ingoing Bound Wave (IBW), an Outgoing Bound Wave (OBW) and an Outgoing Free Wave (OFW), i.e., the combination [IBW, OBW, OFW].

In experimental facilities, reproducing this ideal wave field up to second-order requires an accurate second-order generation with active wave paddle absorption. If second-order wave generation is not available or the active absorption system cannot entirely absorb the OFW, the free-wave contamination is a noticeable amount of unwanted energy propagating shoreward as a free wave (IFW). As a result, superharmonics and subharmonics of the primary frequencies will consist of the combination [IBW, IFW, OBW, OFW], instead of the expected combination [IBW, OBW, OFW]. Therefore, in practical terms, improving a wave generation ultimately requires the attenuation of unwanted $IFWs$.

In this paper, a Generation–Separation–Compensation (GSC) procedure is proposed to firstly, identify and quantify the presence of unwanted $IFWs$ (assessment of the wave generation) and secondly, to attenuate the unwanted $IFWs$ at the generation. This GSC procedure is performed in the following steps:

1. Initial wave generation based on a first-order input ($\eta^{(I)}$) and measurement of the resulting wave field along a dense array of in-line probes.
2. Identification and quantification of the unwanted energy content at the target frequency. At the target frequency (superharmonic or subharmonic of the primary frequencies), any existing IFW is separated by means of the general framework for wave separation that will be explained in Section 3. Therefore, its cross-shore amplitudes (A_x^{IFW}) and phases (ψ_x^{IFW}) should be known at this stage.
3. Back propagation of the separated IFW to the wave-maker location x_0 ($x = 0$ m). At x_0, the initial amplitude and phase are computed as:

$$A_0^{IFW} = \frac{A_x^{IFW}}{K_{s,x}}, \tag{1}$$

and

$$\psi_0^{IFW} = \psi_x^{IFW} + \int_0^x k_F \, dx, \tag{2}$$

where K_s is the linear shoaling coefficient and k_F is the wavenumber of freely propagating waves at the target frequency.

4. Update of the original first-order wave-generation input ($\eta^{(I)}$) by adding a Compensating Wave (CW) at the target frequency. This new wave-generation input is $\eta^{(II)} = \eta^{(I)} + CW$, where the initial amplitude and phase of the CW are:

$$A_0^{CW} = A_0^{IFW} \tag{3}$$

and

$$\psi_0^{CW} = \psi_0^{IFW} + \pi. \tag{4}$$

As a result of these steps, note that each wave condition needs to effectively be run twice per target frequency: Firstly, without the compensation ($\eta^{(I)}$), and secondly, with the compensation ($\eta^{(II)}$). The interaction between the IFW and the CW results in a destructive interference at the wave-maker. Ideally, no unwanted IFW propagates shoreward at the target frequency in the wave field generated by $\eta^{(II)}$. The effectiveness of the GSC procedure will be discussed later on.

3. Summary of the general framework for wave separation

The general framework for wave separation in the frequency domain proposed by PA2020 consists of a qualitative and a quantitative analysis. The qualitative analysis (steps 1–4 below) provides useful information about the number of existing wave trains at the target frequency, the nature of these wave trains (bound or free), their propagation direction (ingoing or outgoing) and their relative importance. The quantitative analysis (step 5 below) consists in a wave separation method. This separation method assumes the target frequency to be formed of the combination [IBW, IFW, OBW, OFW].

In general, PA2020 consider cross-shore and long-shore wave propagation (see Fig. 3 in PA2020). In this paper, we consider one dimensional propagation in the cross-shore direction only (x-axis). Based on this simplification, the general framework for wave separation in the frequency domain is to be applied as follows for each target frequency:

1. *Observation of the cross-shore wave amplitude at the target frequency*. This step aims to identify different node–antinode patterns of the wave amplitude along the spatial domain (x-axis).
2. *Estimation of the existing wave trains*. A first guess of the number n of wave trains at the target frequency based on the observation of N^* different node–antinode patterns is

$$n \geq \lceil (1 + \sqrt{1 + 8N^*})/2 \rceil, \tag{5}$$

where the operator $\lceil \cdot \rceil$ rounds the element to the nearest higher integer.
3. *Identification of the free or bound nature of the wave trains and their relative propagation direction*. Every pair of propagating wave trains, whose wave numbers are k_1 and k_2, creates a node–antinode pattern in the x-axis, if and only if, $k_1 \neq k_2$. In this case, L is the observed distance between consecutive nodes (or antinodes):

$$L^2 = \left(\frac{2\pi}{-(k_1 - k_2)} \right)^2. \tag{6}$$

L is the exact distance between consecutive nodes when the bathymetry is a flat bed, whereas just an approximation for uneven beds. Note that for a wave train j, $k_j = |\vec{k}_j| \cos(\theta_j)$. $|\vec{k}|$ depends on the nature of the wave train (free or bound), whereas θ depends on the propagation direction ($\theta = 0$ if ingoing; $\theta = \pi$ if outgoing).
In general, a variety of pairs of wave trains may exist defining their own distances between consecutive nodes (or antinodes). Therefore, for each observed node–antinode pattern in step 1, the nature and propagation direction of the pair of wave trains are the ones leading to the computed L that better explains its observed distance between nodes.
4. *Relative importance of the wave trains*. In a time–space contour plot, the dominant wave train is the one whose time–space trajectory better matches with the overall trajectory of the surface elevation crests at the target frequency. The relative importance of the remaining wave trains is given by the relative amplitude of the node–antinode patterns that those wave trains forms with the dominant wave train, respectively.
5. *Wave separation*. This method provides the cross-shore wave amplitudes and phases of the wave trains: IBW, OBW, IFW, OFW. The performance of the method depends on the following wave separation settings: number of probes forming the local array (P) and spatial resolution of the local array (Δx_{sep}). PA2020 recommend $4 \leq P \leq 10$ and $0.1\lambda_j < \Delta x_{sep} < 0.3\lambda_j$, where λ_j is the wavelength of each wave train j.
6. *Validation of the wave separation based on the spatial distribution of the nodes and antinodes*. After step 5, the initial phases of the wave trains are known, i.e., [ψ_0^{IBW}, ψ_0^{OBW}, ψ_0^{IFW}, ψ_0^{OFW}]. Therefore, the spatial locations of the antinodes (x_{anti}) and the nodes (x_{node}) may be computed as

$$\int_0^{x_{anti}} \left(\frac{\cos(\theta_1)}{c_1(x)} - \frac{\cos(\theta_2)}{c_2(x)} \right) dx = -\frac{2\pi m - (\psi_1 - \psi_2)}{\omega}, \tag{7}$$

and

$$\int_0^{x_{node}} \left(\frac{\cos(\theta_1)}{c_1(x)} - \frac{\cos(\theta_2)}{c_2(x)} \right) dx = -\frac{\pi(2m+1) - (\psi_1 - \psi_2)}{\omega}, \tag{8}$$

with $m \in \mathbb{Z}$ and c_j being the celerity of each wave train j.
The comparison between the observed locations (step 1) and the computed locations (step 6) of the nodes (or antinodes) will determine the validity of the wave separation (step 5). When the differences are below a certain tolerance, the separated wave trains are considered valid. Otherwise, the separated wave components needs re-computing by modifying the wave separation settings (P, Δx_{sep}).

This scheme is, in principle, applicable to low and high frequencies, i.e., long or short waves, of numerical or experimental water surface elevations when the following requirements about the spatial resolution are fulfilled: First, the cross-shore resolution of the data set (Δx) must satisfy $\Delta x \leq L/2$ in order to identify any node–antinode pattern whose mean distance between antinodes is L. Second, the spatial domain must include at least one node and one antinode. Therefore, the distance between the first probe (x_1) and the last one (x_{end}) must satisfy $|x_{end} - x_1| \geq L/2$.

4. Results

4.1. Assessment of the wave generation

In this subsection, we assess the wave generation of two experimental wave conditions by means of the wave separation of superharmonics (short waves) and subharmonics (long waves) of the primary frequencies. For short waves, we assess the wave generation of the monochromatic wave condition M3 presented in Alsina et al. (2020). For long waves, we assess the wave generation of the bichromatic wave condition B1025 A presented in Baldock et al. (2000). Note that, as M3 and B1025 A are prior to the present paper, the GSC procedure was only used to assess the quality of the wave generation and the presence of free-wave contamination.

4.1.1. Short waves

The wave condition M3 presents a monochromatic wave case propagating on a flat bed of 0.3 m water depth. The period of the monochromatic train is 1.5 s, i.e., the primary frequency is $f_1 \approx 0.667$ Hz, and the initial wave amplitude is 0.035 m. M3 was measured in a medium scale wave flume, iCIEM, at the Universitat Politècnica de Catalunya. This is a flume whose length is 16 m, with a width of 0.40 m and a working

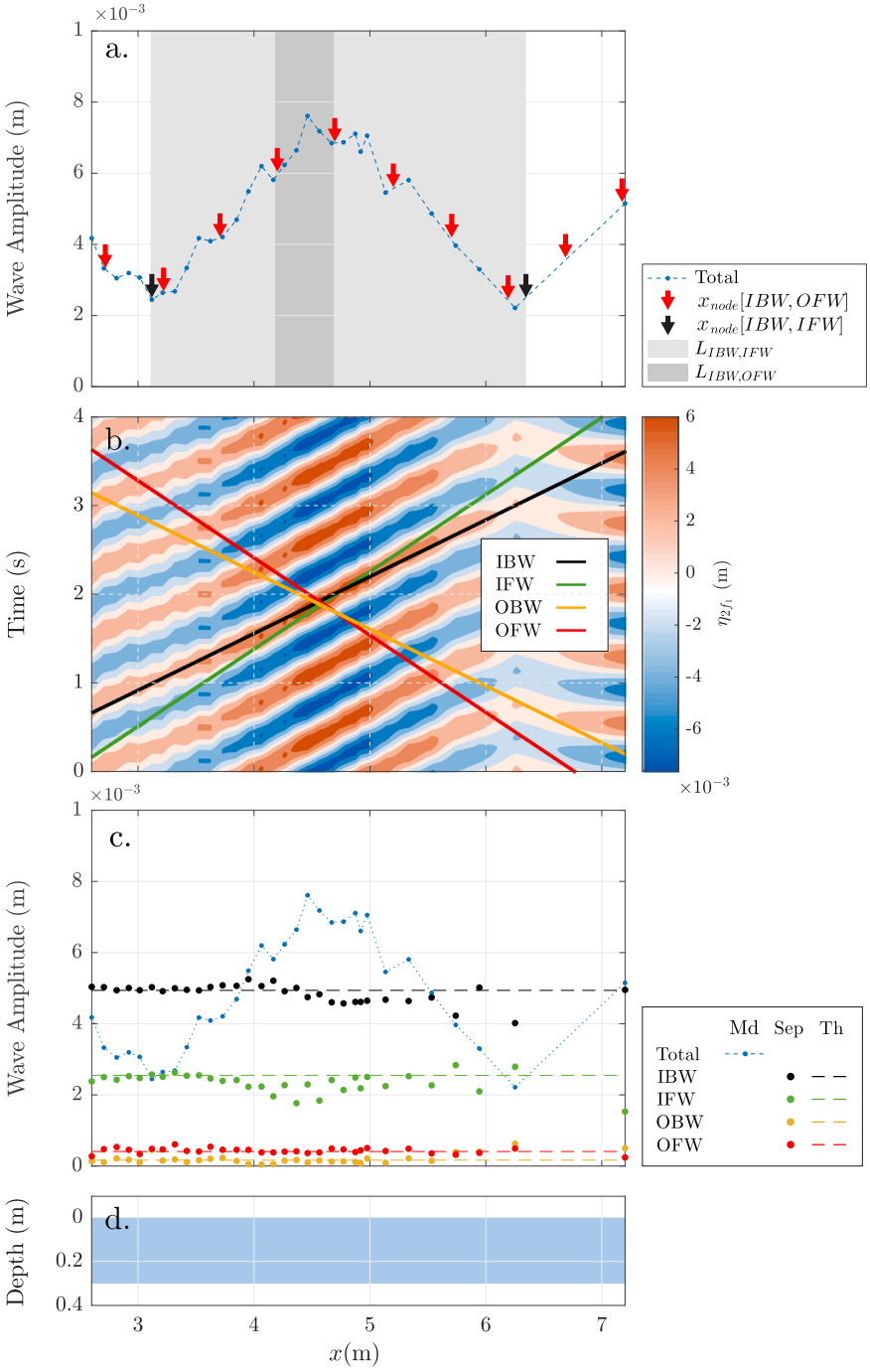

Fig. 1. Plot *a* shows the cross-shore evolution of the total wave amplitude at $2f_1$. X_{anti} $[IBW, OFW]$ (red arrows) and X_{anti} $[IBW, IFW]$ (black arrows) are the set of computed locations of the antinodes belonging to the pairs $[IBW, OFW]$ and $[IBW, IFW]$, respectively. $L_{IBW,IFW}$ (light shaded area) and $L_{IBW,OFW}$ (dark shaded area) are the flat-bed approximation of the mean distance between antinodes. Plot *b* shows the η_{2f_1} contour plot where the time–space trajectories of IBW (black), IFW (green), OBW (yellow) and OFW (red) are displayed. Plot *c* shows the theoretical (Th) and separated (Sep) wave amplitude of $[IBW, IFW, OBW, OFW]$, compared to the measured (Md) total wave amplitude at $2f_1$. Plot *d* illustrates the cross-shore water depth. Dots illustrate the location of the probes. (For interpretation of the references to colour in this figure legend, the reader is referred to the web version of this article.)

water depth of 0.30 m. A dissipative beach made of synthetic foam was placed at the flume end opposite to the wave generation in order to minimize reflections. The wave generation system comprises a piston-type wave paddle where first-order wave generation and no active wave absorption were used. The water surface elevation is measured using resistance-type wave gauges whose averaged spatial resolution is $\Delta x \approx 0.15$ m. The location of these probes is illustrated with dots in Fig. 1.

Fig. 1 illustrates the wave separation of the superharmonic $2f_1$. Fig. 1-*a* shows the cross-shore wave amplitude at $2f_1$ where two node–antinode patterns are noticeable. Consequently, at least three wave trains should exist according to Eq. (5). The larger pattern is the one whose nodes are highlighted in black arrows. The distance between these nodes, estimated as $L_{IBW,IFW} = 3.25$ m by Eq. (6), confirms that this pattern corresponds to the propagation of an incident wave (IBW) that travels bound to the primary wave and an incident free wave (IFW), i.e., the pair $[IBW, IFW]$. The second node–antinode

pattern is weaker with its nodes marked in red arrows. This second undulation is due to the pair $[IBW, OFW]$ as confirmed by the estimation $L_{IBW,OFW} = 0.5$ m. Note that the latter pattern is only noticeable as long as the spatial resolution fulfils the requirement $\Delta x < L_{IBW,OFW}/2$, i.e., noticeable until $x = 5.5$ m.

Fig. 1-*b* shows a contour plot of the surface elevation at $2f_1$ (η_{2f_1}), alongside with the estimated time–space trajectories of IBW, IFW, OBW and OFW. The estimated time–space trajectory of IBW (black solid line) matches with the propagation trajectory of η_{2f_1}. This match confirms that the IBW is the dominant wave train. Moreover, there is a relative difference in the amplitude of the two observed node–antinode patterns. The amplitude of the undulation associated to $[IBW, IFW]$ is larger than the one associated to $[IBW, OFW]$. This relative difference indicates that the wave amplitude of IFW is larger than OFW. Therefore, $A_{IBW} > A_{IFW} > A_{OFW} > A_{OBW}$ at every single location, which is confirmed by the outcomes from the wave separation in Fig. 1-*c*. The energy content of the OBW is negligible.

Fig. 1-*c* shows the outcomes from the wave separation. Based on this wave separation, a summary of the initial amplitudes and phases is presented in Table 1. The wave separation settings are $P = 9$ and $\Delta x_{sep}/\Delta x = 2$, i.e., an average spatial separation resolution of $\Delta x_{sep} = 0.297$ m. Moreover, $\Delta x_{sep}/\lambda \approx 0.18$, which is between 0.05 and 0.45 as recommended by Goda and Suzuki (1976). As a result, the stability of the separation is clear in Fig. 1-*c*. The cross-shore wave amplitudes of the IBW, IFW, OBW and OFW do not undergo any growth, i.e., being practically constant, as expected when propagating on a flat bed. Based on the initial phases in Table 1, the spatial distribution of the nodes is estimated using Eq. (8) for both undulations (marked in red and black arrows in Fig. 1-*a*). The good agreement between the observed and computed locations of the nodes validates the outcomes from the wave separation.

In summary, the GSC procedure allows the assessment of the wave generation by quantifying the presence of spurious waves in the form of IFWs. The potential application of the full GSC procedure to the wave condition M3, i.e., including the attenuation of the IFWs, may result in the reduction of the undesired cross-shore undulations.

4.1.2. Long waves

The wave condition B1025 A presents a bichromatic wave case propagating on a wave flume 18 m long, which comprises a flat bed segment of 5.65 m long and 0.8 m water depth, followed by a 1:10 sloping bed (8 m long until the shoreline). The primary frequencies are $f_1 = 1.123$ Hz and $f_2 = 0.879$ Hz, whose amplitudes are 0.025 m. The resulting group frequency f_g is 0.244 Hz. Waves were generated by a hydraulically driven wedge type wave paddle using second-order generation for long waves alongside with a wave absorption system (see Baldock et al. (2000) for more details). At the beach end (inner surf and swash zones), the bed was made of a rigid polyethylene sheet whose reflection coefficients ranged from 0.9 to 0.6 for unbroken regular waves with frequencies between 0.1 to 0.4 Hz. The water surface elevation is measured using resistance-type wave gauges whose averaged spatial resolution is $\Delta x \approx 0.32$ m. The location of these probes is illustrated with dots in Fig. 2.

Fig. 2 illustrates the separation of the existing long wave trains at the group frequency f_g. Fig. 2-*a* shows the cross-shore wave amplitude at f_g where a very well defined node–antinode pattern exists (the one whose antinodes are marked in the red arrows). In this case, Eq. (5) would indicate that only two wave trains propagate within f_g. However, there is what seems to be an anomalous behaviour of the amplitude at the node around $x = 7$ m compared to the adjacent nodes around $x = 5$ m and $x = 9.5$ m. Assuming that this anomaly belongs to a longer secondary node–antinode pattern, Eq. (5) suggests the existence of at least three wave trains. This assumption will be confirmed later on by the outcomes of the wave separation.

In Fig. 2-*a*, the observed distance between consecutive antinodes marked in red arrows is well explained by the approximation $L_{IBW,OFW}$. This means that a group-bound IBW and an OFW coexist. As seen in Janssen et al. (2003), the IBW travels shoreward with the linear theory group velocity of the primary waves at the mean primary frequency f_p ($f_p = (f_1 + f_2)/2$). The OFW travels seaward with the linear theory velocity that fulfils the Dispersion Equation at f_g.

The undulation due the pair $[IBW, OFW]$ is also clear in Fig. 2-*b*. The dominant trajectory of the surface elevation at f_g (η_{fg}) follows the time–space trajectory of the OFW (red solid line). Therefore, the OFW dominates over the IBW. At this stage, no more reliable information may be inferred about the secondary node–antinode or the nature of the third wave train. However, considering this third wave train to be an IFW is a reasonable guess that will be confirmed by the outcomes of the wave separation.

Fig. 2-*c* shows the outcomes from the wave separation, whose initial amplitudes and phases are presented in Table 1. The wave separation settings are $P = 5$ and $\Delta x_{sep}/\Delta x = 3$ ($\Delta x_{sep}/\lambda$ in the range 0.1–0.45). These settings allow the stability of the separation. The separated (Sep) cross-shore amplitudes for the IBW, IFW and OFW are in good agreement with their theoretical (Th) cross-shore growth. The theoretical evolution for the free waves (IFW and OFW) is based on linear shoaling, whereas the evolution of the bound waves is $A^{IBW} \propto h^{-\alpha}$ as observed by Battjes et al. (2004) and Van Dongeren et al. (2007). For the latter, α converges to 1.15 in no more than 3 iterations (not showed).

The good match between the observed and computed locations of the antinodes (red arrows in Fig. 2-*a*) validates the outcomes of the wave separation. Therefore, the existence of a dominant OFW propagating in conjunction with a group-bound IBW and an IFW is confirmed. The energetic content of the OBW is negligible.

In summary, the wave condition B1025 A presents a very low level of free-wave contamination (low energy content of the IFW). Baldock et al. (2000) estimate the efficiency of the active wave absorption system to be of 90% for frequencies above 0.4 Hz and 60% for frequencies below 0.1 Hz. Therefore, the identified IFW is assumed to be the result of re-reflections at the wave paddle. Note that the wave separation method proposed by PA2020 is not formulated to be used at the surf zone. Therefore, the validity of the separation from $P/2$ probes ($P = 5$ in this case) before the breakpoint onset shoreward must be carefully considered.

Table 1
Outcomes from the wave separation of Figs. 1 and 2: Wave amplitudes and phases of the IBW, IFW, OBW and OFW at x_0.

		IBW	IFW	OBW	OFW
Fig. 1	A_0 (m)	$5 \cdot 10^{-3}$	$2.5 \cdot 10^{-3}$	$1.4 \cdot 10^{-4}$	$3.4 \cdot 10^{-4}$
	ψ_0 (rad)	1.83	4.76	3.64	1.36
Fig. 2	A_0 (m)	$7.31 \cdot 10^{-4}$	$1.2 \cdot 10^{-3}$	$1.75 \cdot 10^{-4}$	$4.5 \cdot 10^{-3}$
	ψ_0 (rad)	4.97	6.22	3.52	3.02

4.2. Improvement of the wave generation

In this subsection, we use the GSC procedure to improve the wave generation of experimental wave conditions belonging to two data sets: *IBIMS-ICL* and *DIFFREP-ICL*. Before using the GSC procedure, the wave generation of these data sets consisted of a first-order force-control wave generation including active wave absorption (Spinneken, 2010). The efficiency of the active wave absorption system is known to reduce as the wave frequency reduces. Therefore, the presence of spurious waves at low frequencies (f_g and subharmonics of f_g) is partially attributed to the first-order wave generation, and partially attributed to the re-reflected long waves at the wave paddle.

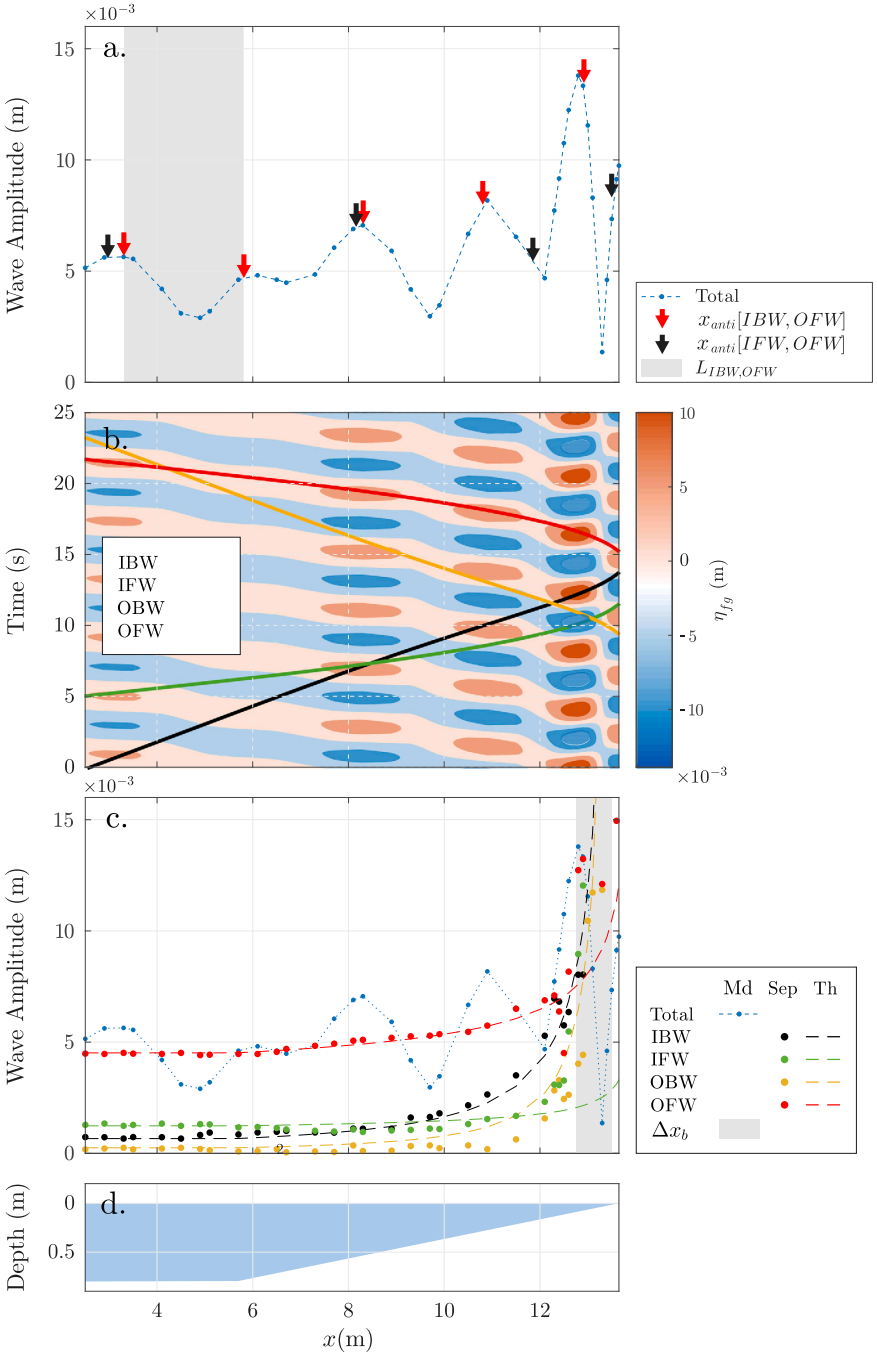

Fig. 2. Wave case B1025 A. Plot *a* shows the cross-shore evolution of the total wave amplitude at f_g. X_{anti} $[IBW, OFW]$ (red arrows) and X_{anti} $[IFW, OFW]$ (black arrows) are the set of computed locations of the antinodes belonging to the pairs $[IBW, OFW]$ and $[IFW, OFW]$, respectively. $L_{IBW,OFW}$ (shaded area) is the flat-bed approximation of the mean distance between antinodes. Plot *b* shows the η_{f_g} contour plot where the time–space trajectories of IBW (black), IFW (green), OBW (yellow) and OFW (red) are displayed. Plot *c* shows the theoretical (Th) and separated (Sep) wave amplitudes of $[IBW, IFW, OBW, OFW]$, compared to the measured (Md) total wave amplitude at f_g. The shaded area in plot *c* highlights the measured breakpoint excursion (Δx_b). Plot *d* illustrates the cross-shore water depth. Dots illustrate the location of the probes. (For interpretation of the references to colour in this figure legend, the reader is referred to the web version of this article.)

4.2.1. *Applying the GSC procedure at the group frequency*

Twelve bichromatic wave conditions compose the *IBIMS-ICL* data set (Padilla and Alsina, 2017). For a range of group frequencies, these wave conditions are designed in such a way that all the wave groups are identical within a time series, i.e., the repetition period T_r between two identical phases matches the group period T_g (see Fig. 3, where $T_r = T_g$). Consequently, the group frequency f_g is the only existing energetic low frequency. The primary frequencies are f_1 and f_2. See Padilla and Alsina (2017) or Appendix A for a summary of the characteristics of the wave conditions.

Fig. 4 shows the experimental wave condition B-1, where the surf zone is not included. The measured cross-shore amplitude evolution at f_g and the separated wave trains (IBW, OFW, IFW) are illustrated before (plots *a* and *b*) and after (plots *c* and *d*) the GSC procedure is applied. As expected from such mild sloping bed (see plot *e*), the separated OBW has a negligible energy content and has not been displayed.

Before applying the GSC procedure, two clear node–antinode patterns may be identified in Fig. 4-*a*. Hence, at least three different wave trains coexist at f_g according to Eq. (5). The antinodes whose average

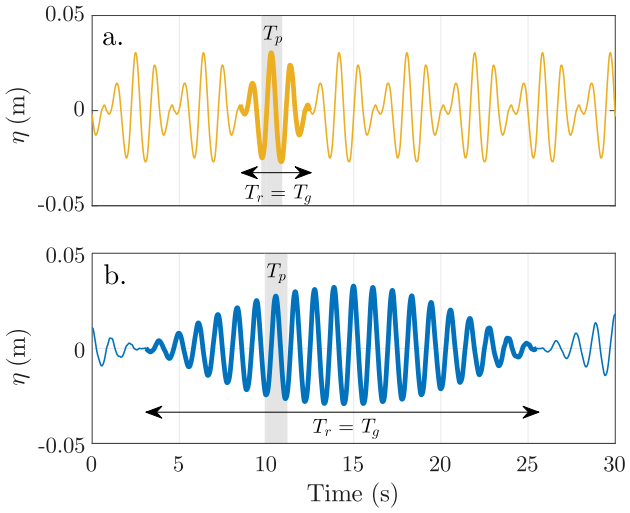

Fig. 3. Water surface elevation at x_1 (closest probe to the wave-maker) for wave conditions B-1 (*a*) and B-4 (*b*). The thicker line highlights an individual wave group within the time series. The wave group period T_g matches the repetition period T_r. T_p is the mean period of the short individual waves (shaded area).

Table 2
Amplitudes and phases obtained at x_0 (wave-maker) of the existing wave trains at f_g for the experimental wave case *B-1* (*IBIMS-ICL* data set) before and after applying the GSC procedure.

	Before GSC	After GSC
A_0^{IBW} (m)	5.66 $\cdot 10^{-4}$	5.51 $\cdot 10^{-4}$
ψ_0^{IBW} (rad)	3.41	3.47
A_0^{IFW} (m)	2.59 $\cdot 10^{-4}$	0.25 $\cdot 10^{-4}$
ψ_0^{IFW} (rad)	4.48	4.51
A_0^{OFW} (m)	1.57 $\cdot 10^{-4}$	1.65 $\cdot 10^{-4}$
ψ_0^{OFW} (rad)	2.34	3.06

distance is $L = \mathcal{O}(10$ m) correspond to the linear superposition of the pair $[IBW, IFW]$. The antinodes whose distance is $L = \mathcal{O}(1$ m) correspond to the linear superposition of the pair $[IBW, OFW]$. Since the amplitude of the antinodes belonging to $[IBW, IFW]$ is larger than the associated to $[IBW, OFW]$, then $A^{IFW} > A^{OFW}$. All this is consistent with the separated IBW, IFW and OFW. Both IFW and OFW behave as free waves whose growth follows linear shoaling. In contrast, the growth of the IBW is very well described as proportional to $h^{-\alpha}$, where $\alpha \approx 1.05$ in this particular case. Likewise, the IBW is, as expected, in antiphase with the envelope of the high frequency wave group (Fig. 4-*b* and *d*).

After applying the GSC procedure, only one node–antinode pattern is observed at the cross-shore wave amplitude (Fig. 4-*c*). This pattern corresponds to the propagation of the pair $[IBW, OFW]$. In Fig. 4-*c*, the negligible wave amplitude of the IFW confirms its effective attenuation. Table 2 shows the amplitude and phase of the separated wave trains back-propagated to x_0 before and after applying the GSC procedure. The initial amplitudes of the IBW and the OFW are seen to remain practically the same. The IFW amplitude has been importantly reduced, with an attenuation of around 90%.

Fig. 5 verifies a proper attenuation of the IFW throughout all the experimental wave cases in *IBIMS-ICL* data set. This figure shows the absolute (plot *a*) and relative (plot *b*) damping of the IFW at f_g after applying the GSC procedure. In absolute terms, the IFW amplitude after the GSC procedure is $\mathcal{O}(10^{-4}$ m). In relative terms, this damping means an overall attenuation of above 60% of the spurious energy, increasing to nearly 90% for some cases.

4.2.2. Applying the GSC procedure at subharmonics of the group frequency

Ten bichromatic wave conditions compose the *DIFFREP-ICL* data set (Padilla and Alsina, 2018). These wave conditions are designed in such a way that the ratio between the repetition period T_r and the group period T_g is a positive integer number Rp, i.e., Rp is the number of wave groups before a given wave phase repeats exactly (see Fig. 6 for cases with $Rp = [2, 3$ and $5]$). The group frequency f_g is no longer the only energetic low frequency (as it was with *IBIMS-ILC* data set). Subharmonics of f_g, like the repetition frequency f_r $(1/T_r)$, are also energetic frequencies. As a consequence, an accurate long wave generation of the cases forming *DIFFREP-ICL* data set requires the attenuation of the free-wave contamination at the group frequency and further lower frequencies. See Padilla and Alsina (2018) or Appendix B for a summary of the characteristics of the wave conditions.

Fig. 7 shows the wave case MR-03 ($Rp = 3$) before and after applying the GSC procedure. The target wave frequencies in this case are the subharmonics f_g, $2f_r$ and f_r. Before applying the GSC procedure (left-hand side plots in Fig. 7), the existence of IFWs at f_g, $2f_r$ and f_r is evident because of the observed node–antinode patterns and confirmed by the separated wave trains. After applying the GSC procedure, important differences are observed when comparing the cross-shore wave amplitude in plots *a-c* with plots *e-g*, respectively. At f_g, the node around $x = 5$ m and the antinode around $x = 25$ m observed in plot *a* vanish in plot *e*. As a result, the cross-shore wave amplitude in plot *e* is almost entirely explained by a dominant IBW (the OFW is practically negligible). At $2f_r$ and f_r, there is no propagating IBW and the observed node–antinode patterns in plot *b* and *c* are due to each pair $[IFW, OFW]$. In plots *f* and *g*, these node–antinode patterns are importantly reduced once the respective IFWs are attenuated. In relative terms, the IFW attenuation is 88.26% at f_g, 80.63% at $2f_r$ and 89.12% at f_r for the wave condition MR-03.

It is important to mention that the attenuation of the IFW at any of the above subharmonics is experimentally observed to have implications in the rest. Therefore, in practical terms, the GSC procedure is to be applied individually at each subharmonic in an energetic-descending order. The IFW is suppressed at f_g in the first place, followed by $2f_r$ and f_r.

Fig. 8 verifies a proper attenuation of the free-wave contamination throughout all the experimental wave cases in *DIFFREP-ILC* data set. Fig. 8 displays the IFW attenuation at f_g and f_r since those were the frequencies of interest in Padilla and Alsina (2018). At f_g, the overall attenuation is above 90% (see plot *c*) and the resulting IFW amplitude after applying the GSC procedure is $\mathcal{O}(10^{-4}$ m) (plot *a*). At f_r, the overall attenuation is above 60% (plot *d*). This represents a decay in the efficiency to suppress the unwanted energy at f_r compared to f_g. Although, the wave amplitude of the IFW at f_r ($\mathcal{O}(10^{-5}$ m)) is an order of magnitude below the wave amplitude of the IFW at f_g.

5. Discussion

Free-wave contamination is a relatively common and undesired issue in many experimental facilities. Free-wave contamination is the combination of spurious waves from different sources. These spurious waves are partially the result of first-order wave-makers being unable to correctly reproduce the target wave field, and partially, re-reflections of outgoing waves at the paddle board of the wave-maker. Traditionally, the implementation of second-order wave generation theory is supposed to overcome the former (Van Dongeren et al., 2002), whereas the use active wave absorption systems is supposed to overcome the latter (Lykke Andersen et al., 2016, 2018). Unfortunately, it is difficult to completely eliminate the free-wave contamination and it usually remains unnoticed when the effectiveness of, mainly, the active wave absorption systems is taken for granted.

Active wave absorption systems absorb a good part of the outgoing wave energy content. To do so, these systems generate a compensating wave in real time that is meant to cancel out the re-reflection of the

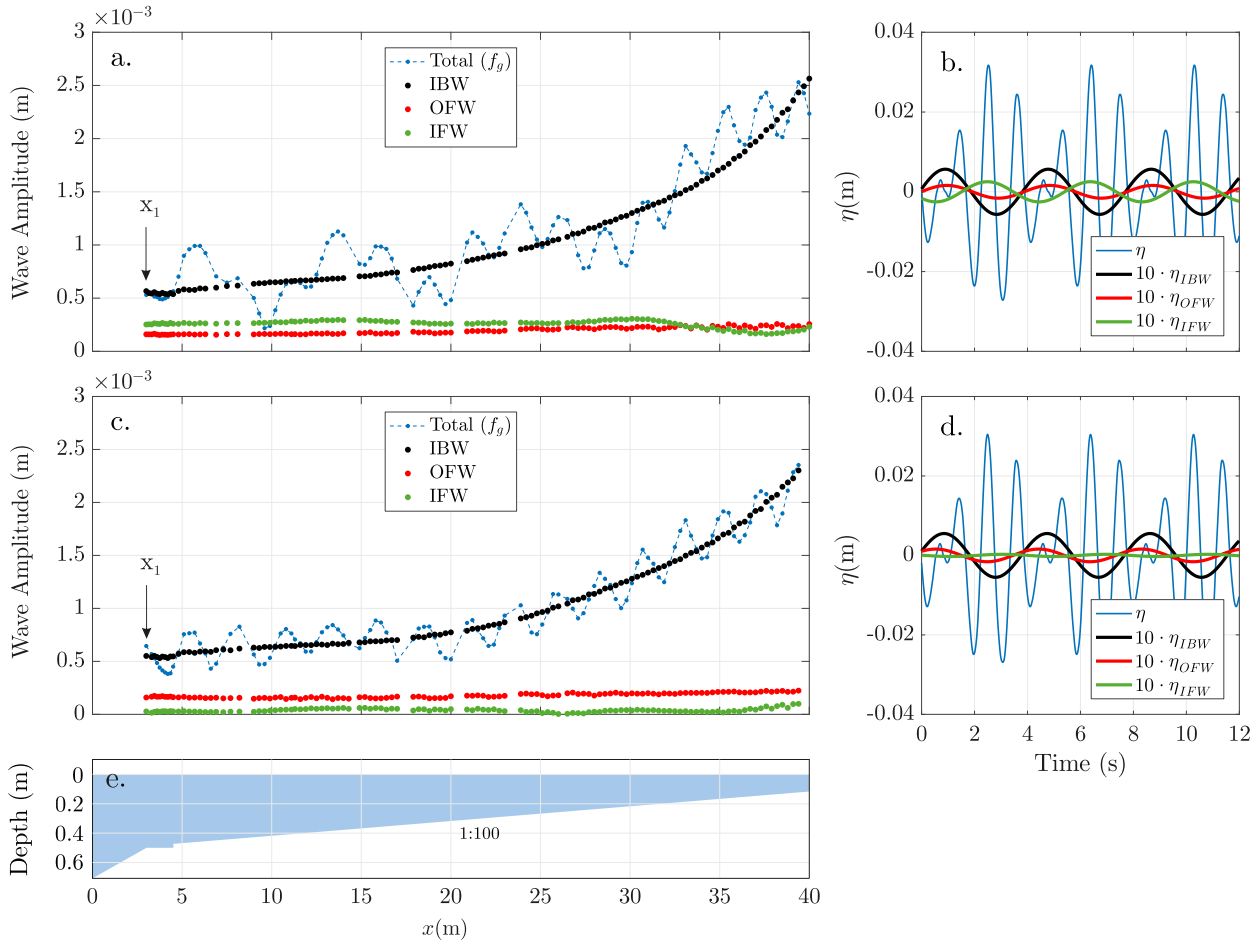

Fig. 4. Wave condition B-1 before (plots *a* and *b*) and after (plots *c* and *d*) applying the GSC procedure at f_g. Plots *a* and *c* show the cross-shore evolution of the total amplitude at f_g and the separated wave trains (IBW, OFW and IFW). Plots *b* and *d* show the water surface elevation time series at x_1 with the separated wave trains at f_g multiplied by a factor of 10. The wave separation settings are [$P = 15$, $\Delta x_{sep}/\Delta x = 3$]. Plot *e* illustrates the cross-shore water depth. Dots illustrate the location of the probes.

outgoing wave at the paddle board. These systems yield a frequency-dependent absorption rate that may be up to 90% within the target frequency band, with rapid decay outside this band (Lykke Andersen et al., 2016). In practice, the actual effectiveness of these systems is usually unknown. If no active wave absorption is used, a purely re-reflected wave can be identified since it has to be in phase with the outgoing wave at the paddle board. If active wave absorption is used, a residual wave arises as the sum of the re-reflected wave and the compensating wave. This residual wave is not necessarily in phase with the outgoing wave at the paddle board, and consequently, cannot be distinguished from any other existing spurious wave. Outside the target frequency band where the effectiveness of the active wave absorption system reduces, these residual waves may become important, being a significant fraction of the existing free-wave contamination. Some studies, such as Barthel and Mansard (1988), Zaman et al. (2010), Orszaghova et al. (2014), Grue and Kolaas (2017) or Padilla (2019), have reported that the influence of free-wave contamination in the shallow water hydrodynamics should not be ignored in experimental studies. In this context, the GSC procedure allows identifying and minimizing the free-wave contamination and may be of interest for most experimental facilities.

The GSC procedure, as described in Section 2, is a useful tool to evaluate the accuracy of wave generation and wave absorption systems. Applying this GSC procedure provides, in practice, with similar results to a theoretical second-order wave generation with negligible re-reflections. The advantage of the GSC procedure is that it minimizes the free-wave contamination, regardless of the source (first-order wave-generation or re-reflections). Furthermore, this GSC procedure provides with more reliable wave fields since the level of free-wave contamination is quantified before and after applying the GSC procedure. The inconvenience is that the GSC procedure requires being applied to every target frequency individually. This inconvenience is the main limitation when applying the GSC procedure to irregular wave conditions as it is meant to be sequentially applied to every frequency bin in the wave spectrum. This sequential application implies some challenges that would require to be properly addressed: (1) Setting the appropriate frequency bin size as a balance between time cost and accuracy; (2) the iterative application of the GSC procedure to each frequency bin; and (3) considering the potential energy transfer between frequency bins (e.g., between the bins centred at f_i and $2f_i$). If these energy transfers were relevant, the attenuation of the IFW for a certain bin may alter the energy content of some other frequency bins. Therefore, it would be necessary to set the appropriate sequence of frequency bins where to apply the GSC procedure. This effect increases with the number of bins as has already been observed for a limited number of frequencies in Section 4.2.2. On top of that, the framework for wave separation by PA2020 turns less accurate when the number of wave components within a certain frequency is above four, which is likely to happen when working with frequency bins. This extra limitation is extensively discussed in PA2020 when addressing the application of the qualitative and quantitative analysis over irregular wave conditions. Therefore, applying the GSC procedure to irregular waves is a complex topic which is out of the scope of this paper.

The presented experimental wave fields belonging to *IBIMS-ILC* and *DIFFREP-ILC* data sets were carried out in a wave flume where

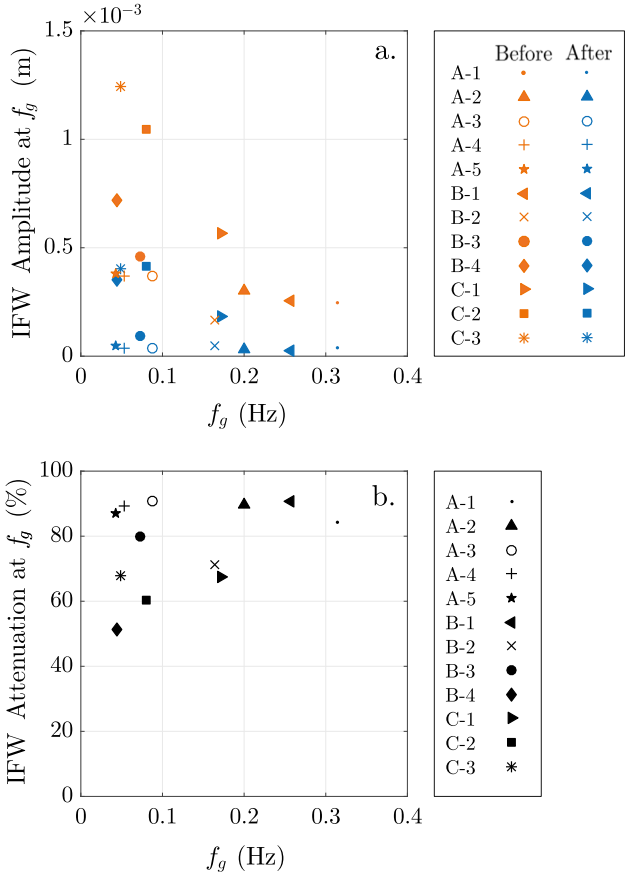

Fig. 5. Plot *a* shows the IFW amplitude at the location x_1 before and after applying the GSC procedure to the wave conditions in *IBIMS-ILC* data set. Plot *b* shows the IFW attenuation percentage.

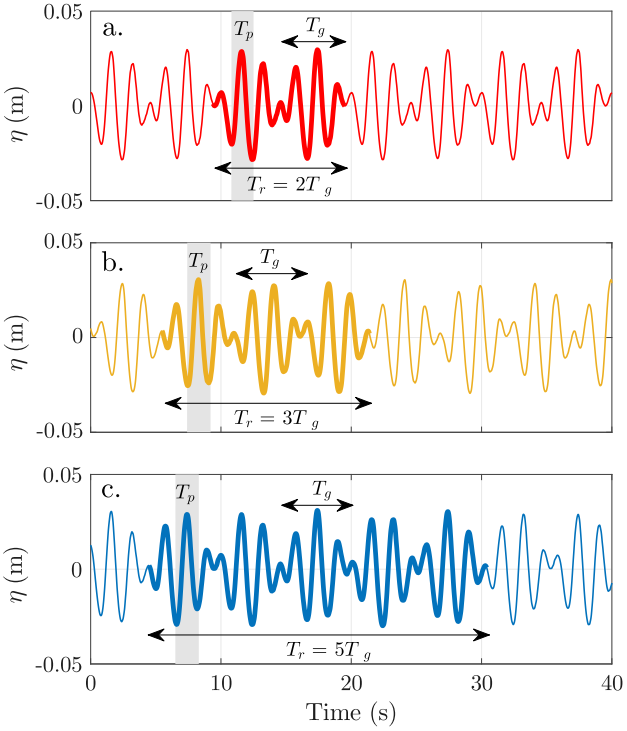

Fig. 6. Water surface elevation η at x_1 for the wave conditions MR-02 (*a*), MR-03 (*b*) and MR-06 (*c*). The thicker line highlights the sequence of Rp wave groups within a repetition period T_r. The wave group period is T_g and the mean period of the short individual waves is T_p (shaded area).

first-order wave generation and active wave absorption, based on force-feedback control, were used Spinneken (2010). This kind of active wave absorption has been reported to effectively reduce the re-reflections at the high frequency domain. However, an important level of free-wave contamination is observed at the low frequency. After using the GSC procedure, the experimental data sets are in very good agreement with the expected second-order wave fields. For those, the attenuation rate of the free-wave contamination is between 60% to 90%.

Reanalysis of previous data (Baldock et al., 2000) have been performed where second-order wave generation and active wave absorption were used. It was detected the presence of a spurious IFW, which is likely to be the residual wave of the OFW not being fully absorbed by the active absorption system. Indeed, Baldock et al. (2000) already reported a decay in the efficiency of active absorption as the wavelength of the OFW increases. The level of free-wave contamination (energy content of the IFW) is low and did not affect the conclusions presented in Baldock et al. (2000). However, the attenuation of this IFW using the proposed GSC procedure could have improved the wave generation reducing potential non-desired influences.

The GSC procedure is reliable as long as (i) the maximum available stroke of the wave-maker is not exceeded and (ii) a minimum spatial domain length and resolution are fulfilled. Assuming the former, the latter is quite relevant to correctly perform the wave separation. In this paper, the general framework for wave separation in the frequency domain proposed by PA2020 has been used due to its suitability for long and short waves propagating on uneven bathymetries. This framework provides with a qualitative analysis to estimate the number of existing wave trains at the target frequency, their nature, propagation direction and relative importance. These outcomes are confirmed by the quantitative analysis (wave separation method). In this paper, the applicability of the qualitative and quantitative analyses over very different spatial resolutions has been tested on a variety of experimental wave conditions.

This paper presents a variety of nonlinear waves propagating over different bathymetries and being measured with very different spatial resolutions. For those wave fields, the number and nature of the existing wave trains at each frequency are a priori unknown. However, when they are more than two, the cross-shore wave amplitude may display observable node–antinode patterns. The qualitative analysis of those patterns, as proposed by PA2020, allows an estimation of the number and nature of the existing wave trains. For the wave fields analysed in this paper, IBW is often the dominant wave train that travel bound to the primary frequencies, IFW is an incident free wave train and OFW is an outgoing free wave train. In general, the qualitative analysis applied to long waves requires longer spatial domains ($\mathcal{O}$(10 m)) than what necessary for short waves ($\mathcal{O}$(1 m)), but the spatial resolution does not really need to be as dense. An averaged Δx around 0.4 m was used to capture the undulations at subharmonics of the primary frequencies. An averaged Δx around 0.1 m was used for the superharmonics.

Having a wave field measured with a uniform spatial resolution is typical of theoretical and numerical wave data. However, this is not usually the case for experimental and field wave data, where the number of available probes are limited. In these cases, a changing spatial resolution offers higher resolution at locations of interest. This lack of uniformity does not affect the quantitative analysis (wave separation method), which is seen to work with probes having different distances between each other. The resolution of the local array is not constant and $\Delta x_{sep}/\lambda$ operates over a range. In the present analysis, $\Delta x_{sep}/\lambda$ is in the range 0.1–0.45, which is in agreement with the recommended threshold proposed by Goda and Suzuki (1976) to guarantee the stability of the separation. As a result, the outcomes from the wave

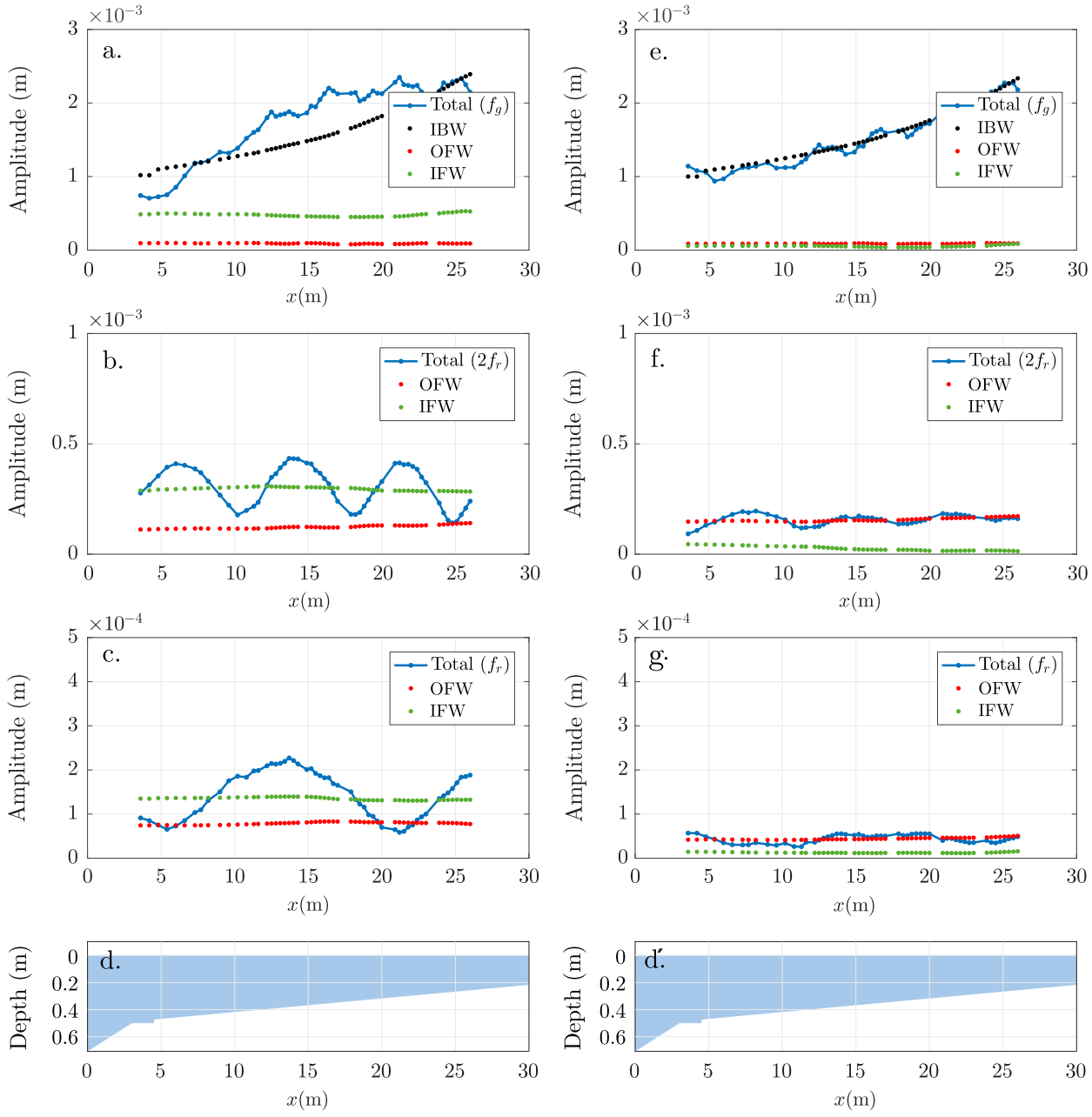

Fig. 7. Wave case *MR-03* belonging to *DIFFREP-ICL* data set before (left-hand side plots) and after (right-hand side plots) sequentially applying the GSC procedure. For the signals $\eta^{(I)}$ (plot a) and $\eta^{(IV)}$ (plot e), the cross-shore amplitude of the total signal at f_g and its separated components (IBW, IFW, OFW) are showed. Similarly, plots *b* ($\eta^{(I)}$) and *f* ($\eta^{(IV)}$) show the cross-shore amplitude at $2f_r$, whereas plots *c* ($\eta^{(I)}$) and *g* ($\eta^{(IV)}$) does for f_r. Plots *d* and *d'* illustrate the cross-shore water depth. Dots illustrate the location of the probes.

separation perform a stable solution regardless of their cross-shore changing spatial resolution. Furthermore, the recommended number P of probes forming the local array is seen to lay in the range 5–10. Similar sizes of the local array were used by Battjes et al. (2004), Lin and Huang (2004), Van Dongeren et al. (2007) and Lykke Andersen et al. (2017).

6. Conclusions

Free-wave contamination is a common issue in many experimental wave facilities. Higher order wave generations are often not widely implemented and the effectiveness of active wave absorption systems is usually unknown. In order to minimize the free-wave contamination, this paper presents a Generation–Separation–Compensation (GSC) procedure that effectively (1) identifies and quantifies and (2) attenuates (if needed) the existing free-wave contamination. In practical terms, the resulting wave field after applying the GSC procedure is seen to behave as expected from a higher order wave generation. This accuracy up to second order is seen for the experimental bichromatic wave conditions. For those wave conditions, the attenuation ratio of the low frequency unwanted energy content is usually relatively high (above 60%) and especially high at the group frequency (around 90%).

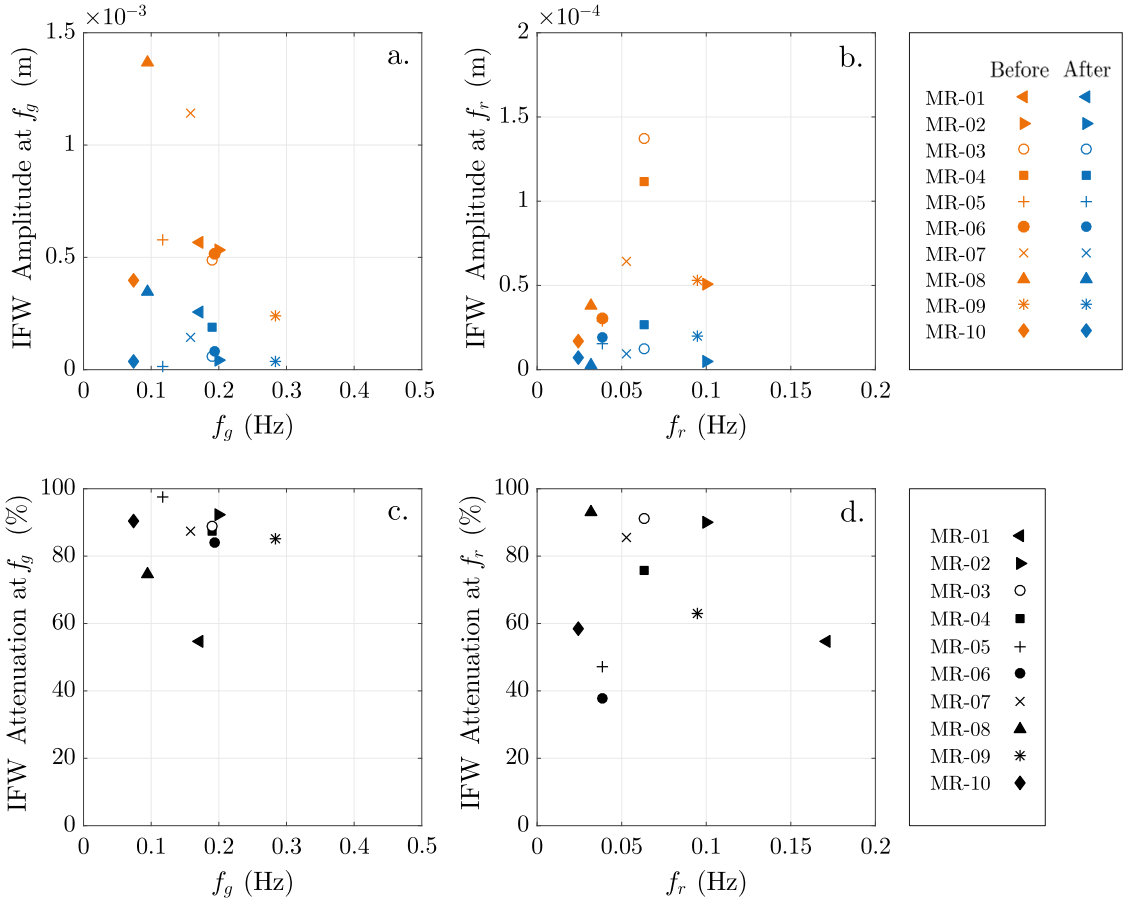

Fig. 8. Plots *a* and *b* show the IFW amplitude at f_g and f_r, respectively, before and after applying the GSC procedure for the wave cases in *DIFFREP-ILC* data set. Plots *c* and *d* show the IFW attenuation percentage at f_g and f_r, respectively. The amplitudes are provided at the first measuring location (x_1).

In order to identify and quantify the level of free-wave contamination, the GSC procedure uses the general framework for wave separation proposed by PA2020. The application over experimental data of this framework for wave separation is presented with excellent results. The robustness of the information provided by the qualitative analysis is guaranteed for wave cases fulfilling a minimum spatial domain length and resolution. Moreover, the stability of the quantitative analysis (wave separation method) is also guaranteed for local arrays formed of more than 5 probes, with $\Delta x_{sep}/\lambda$ typically being in the recommended range of 0.1–0.45.

CRediT authorship contribution statement

Enrique M. Padilla: Conceptualization, Methodology, Software, Validation, Formal analysis, Investigation, Writing – original draft, Writing – review & editing, Visualization. **Jose M. Alsina:** Conceptualization, Investigation, Writing – review & editing, Supervision, Funding acquisition.

Declaration of competing interest

The authors declare that they have no known competing financial interests or personal relationships that could have appeared to influence the work reported in this paper.

Acknowledgements

During this research, the first author was supported with a PhD fellowship from the Department of Civil and Environmental Engineering, Imperial College London, United Kingdom. The authors thank Professor Tom Baldock for providing the data set used in Baldock et al. (2000).

Table 3
Generated bichromatic wave conditions for *IBIMS-ICL* data set.

Case	f_p (Hz)	f_1 (Hz)	f_2 (Hz)	$\Delta f = f_g$ (Hz)	a_1 (m)	N	n	Rp
A-1	1.1	1.257	0.943	0.314	0.015	1	3	1
A-2	1.1	1.200	1.000	0.200	0.015	1	5	1
A-3	1.1	1.144	1.056	0.088	0.015	1	12	1
A-4	1.1	1.127	1.073	0.054	0.015	1	20	1
A-5	1.1	1.122	1.078	0.043	0.015	1	25	1
B-1	0.9	1.029	0.771	0.257	0.015	1	3	1
B-2	0.9	0.981	0.818	0.164	0.015	1	5	1
B-3	0.9	0.936	0.864	0.072	0.015	1	12	1
B-4	0.9	0.922	0.878	0.044	0.015	1	20	1
C-1	0.6	0.686	0.514	0.171	0.015	1	3	1
C-2	0.6	0.640	0.560	0.080	0.015	1	7	1
C-3	0.6	0.624	0.576	0.048	0.015	1	12	1

Appendix A. IBIMS-ICL data set

See Table 3.

Appendix B. DIFFREP-ICL data set

See Table 4.

Table 4
Generated bichromatic wave conditions for *DIFFREP-ICL* data set.

Case	f_p (Hz)	f_1 (Hz)	f_2 (Hz)	$\Delta f = f_g$ (Hz)	f_r (Hz)	a_1 (m)	n	Rp
MR-01	0.6	0.686	0.514	0.171	0.171	0.015	3	1
MR-02	0.6	0.700	0.500	0.200	0.100	0.015	3	2
MR-03	0.6	0.695	0.505	0.189	0.063	0.015	3	3
MR-04	0.6	0.695	0.505	0.189	0.063	0.025	3	3
MR-05	0.6	0.658	0.542	0.116	0.039	0.015	5	3
MR-06	0.6	0.697	0.503	0.194	0.039	0.015	3	5
MR-07	0.5	0.579	0.421	0.158	0.053	0.015	3	3
MR-08	0.3	0.347	0.253	0.095	0.032	0.010	3	3
MR-09	0.9	1.042	0.758	0.284	0.095	0.015	3	3
MR-10	0.6	0.637	0.563	0.074	0.025	0.015	8	3

References

Aknin, D., 2015. Creating a Shallow-Water Experimental Wave Environment (Ph.D. thesis, Doctoral dissertation). Imperial College London.

Alsina, J.M., Jongedijk, C.E., van Sebille, E., 2020. Laboratory measurements of the wave-induced motion of plastic particles: Influence of wave period, plastic size and plastic density. J. Geophys. Res. Oceans 125 (12), e2020JC016294.

Alsina, J.M., Padilla, E.M., Cáceres, I., 2016. Sediment transport and beach profile evolution induced by bi-chromatic wave groups with different group periods. Coast. Eng. 114, 325–340.

Baldock, T., Huntley, D., Bird, P., O'Hare, T., Bullock, G., 2000. Breakpoint generated surf beat induced by bichromatic wave groups. Coast. Eng. 39 (2), 213–242.

Barthel, V., Mansard, E., 1988. Second-order waves—Importance in experiment and nature. Nonlinear Water Waves 323–330.

Battjes, J., Bakkenes, H., Janssen, T., Van Dongeren, A., 2004. Shoaling of subharmonic gravity waves. J. Geophys. Res. Oceans 109 (C2).

Goda, Y., Suzuki, T., 1976. Estimation of incident and reflected waves in random wave experiments. Coast. Eng. Proc. 1 (15).

Grue, J., Kolaas, J., 2017. Experimental particle paths and drift velocity in steep waves at finite water depth. J. Fluid Mech. 810.

Hansen, N.-E.O., Sand, S.E., Lundgren, H., Sorensen, T., Gravesen, H., 1980. Correct reproduction of group-induced long waves. In: Coastal Engineering 1980. pp. 784–800.

Hansen, J.B., Svendson, I.A., 1974. Laboratory generation of waves of constant form. Coast. Eng. Proc. 1 (14).

Janssen, T., Battjes, J., Van Dongeren, A., 2003. Long waves induced by short-wave groups over a sloping bottom. J. Geophys. Res. Oceans 108 (C8).

Kirby, J.T., Özkan-Haller, H.T., Haller, M.C., 2007. Seiching in a large wave flume. In: Coastal Engineering 2006: (in 5 Volumes). World Scientific, pp. 1159–1171.

Kostense, J.K., 1984. Measurements of surf beat and set-down beneath wave groups. In: Coastal Engineering 1984. pp. 724–740.

Lin, C.-Y., Huang, C.-J., 2004. Decomposition of incident and reflected higher harmonic waves using four wave gauges. Coast. Eng. 51 (5–6), 395–406.

Lykke Andersen, T., Clavero, M., Eldrup, M., Frigaard, P., Losada, M., 2018. Active absorption of nonlinear irregular waves. Coast. Eng. Proc. 1 (36), papers.12.

Lykke Andersen, T., Clavero, M., Frigaard, P., Losada, M., Puyol, J., 2016. A new active absorption system and its performance to linear and non-linear waves. Coast. Eng. 114, 47–60.

Lykke Andersen, T., Eldrup, M.R., Frigaard, P., 2017. Estimation of incident and reflected components in highly nonlinear regular waves. Coast. Eng. 119, 51–64.

Madsen, P., Sørensen, O., 1993. Bound waves and triad interactions in shallow water. Ocean Eng. 20 (4), 359–388.

Maguire, A., Ingram, D., 2011. On geometric design considerations and control methodologies for absorbing wavemakers. Coast. Eng. 58 (2), 135–142.

Milgram, J.H., 1965. Compliant Water Wave Absorbers (Ph.D. thesis, Doctoral dissertation). Massachusetts Institute of Technology.

Newman, J., 2010. Analysis of wave generators and absorbers in basins. Appl. Ocean Res. 32 (1), 71–82.

Orszaghova, J., Taylor, P.H., Borthwick, A.G., Raby, A.C., 2014. Importance of second-order wave generation for focused wave group run-up and overtopping. Coast. Eng. 94, 63–79.

Padilla, E.M., 2019. Wave-Group Propagation and Hydrodynamics in the Inner Surf and Swash Zones (Ph.D. thesis, Doctoral dissertation). Imperial College London.

Padilla, E.M., Alsina, J.M., 2017. Transfer and dissipation of energy during wave group propagation on a gentle beach slope. J. Geophys. Res. Oceans 122 (8), 6773–6794.

Padilla, E.M., Alsina, J.M., 2018. Long wave generation induced by differences in the wave-group structure. J. Geophys. Res. Oceans 123 (12), 8921–8940.

Padilla, E.M., Alsina, J.M., 2020. A general framework for wave separation in the frequency domain. Coast. Eng. 103686.

Ruffini, G., Briganti, R., Alsina, J.M., Brocchini, M., Dodd, N., McCall, R., 2019. Numerical modeling of flow and bed evolution of bichromatic wave groups on an intermediate beach using nonhydrostatic xbeach. J. Waterw. Port Coast. Ocean Eng. 146 (1), 04019034.

Schäffer, H.A., 1996. Second-order wavemaker theory for irregular waves. Ocean Eng. 23 (1), 47–88.

Schäffer, H.A., Jakobsen, K., 2003. Non-linear wave generation and active absorption in wave flumes. In: Long Waves Symposium. Thessaloniki, Greece.

Spinneken, J., 2010. Wave Generation and Absorption Using Force-Feedback Control (Ph.D. thesis, Doctoral dissertation). Imperial College London.

Spinneken, J., Swan, C., 2009a. Second-order wave maker theory using force-feedback control. Part I: A new theory for regular wave generation. Ocean Eng. 36 (8), 539–548.

Spinneken, J., Swan, C., 2009b. Second-order wave maker theory using force-feedback control. Part II: An experimental verification of regular wave generation. Ocean Eng. 36 (8), 549–555.

Van Dongeren, A., Battjes, J., Janssen, T., Van Noorloos, J., Steenhauer, K., Steenbergen, G., Reniers, A., 2007. Shoaling and shoreline dissipation of low-frequency waves. J. Geophys. Res. Oceans 112 (C2).

Van Dongeren, A., Klopman, G., Reniers, A., Petit, H., 2002. High-quality laboratory wave generation for flumes and basins. In: Ocean Wave Measurement and Analysis (2001). pp. 1190–1199.

Van Leeuwen, P.J., Klopman, G., 1996. A new method for the generation of second-order random waves. Ocean Eng. 23 (2), 167–192.

Zaman, M.H., Peng, H., Baddour, E., Spencer, D., McKay, S., 2010. Identifications of spurious waves in the wave tank with shallow water. In: 29th International Conference on Ocean, Offshore and Arctic Engineering, Vol. 4. pp. 683–695.